

Numerical Investigation of the Slag Behavior in the Aft-End Cavity of Solid Rocket Motors⁺

Paul Liaw*, Yen-Sen Chen**, and Huan-Min Shang*
Engineering Sciences, Inc., Huntsville, Alabama 35802
and

Denise Doran***
NASA MSFC, Huntsville, Alabama 35812

ABSTRACT

The RSRM geometry at 67 seconds is used for the analysis of the slag behavior in the aft-end cavity using the FDNS (Finite Difference Navier-Stokes) code to obtain a better understanding of the relationship between slag behavior and SRM performance. The FDNS flow solver is a finite difference method for solving Navier-Stokes equations using non-staggered curvilinear grid system with multi-zone multi-block option for multiple species to simulate the complex flow problems. A Lagrangian-Eulerian particle tracking method is employed in the FDNS to provide effects of momentum and energy exchanges between the gas phase and the particle phase. The particle trajectories are calculated using a one-step implicit method. The VOF (Volume of Fluid) method is employed to simulate the slag behavior in the aft-end cavity of the SRM.

The obtained results reveals the potential impact of the particles on the operation of the motor as well as its performance. It is believed that the heat flux and the pressure distributions in the aft-end cavity will cause recirculation and influence the design requirements. The influence will be increased due to the accumulation of the slag in the aft-end cavity. In the present study, the particulate phase was assumed to be aluminum oxide (Al₂O₃) only. The accumulated slag changes the shape of the aft-end cavity and influences the flowfield. The obtained analyses of the flowfield and the slag behavior in the aft-end cavity using the FDNS code in the present research can assist the designers to improve the design of the solid rocket motors.

INTRODUCTION

It is known that the flowfield of the solid rocket motor is very complicated due to the chemical reaction, particle evaporation, combustion, and breakup, and other complex characteristics like agglomeration and coalescence etc. Because the distribution of the particles affects the performance of the motor, the prediction of the

particle effects plays an important role for the SRM design.

Traditionally, metal powders are used in solid propellants for the purpose of increasing the motor specific impulse. High density and high heat of reaction are two factors which contribute to high impulse. It is known that the simulations of internal flowfields of SRM with Al-based propellants require complex multi-phase, turbulent, and chemical reacting flow models. On the other hand, because of relative velocity and temperature difference between particles and the gas flow, inter-phase drag forces and heat transfer exist. Therefore, the effect of particles on the flowfield has a significant impact. The evaporation of the Al and Al₂O₃ transfers the mass from particulate phase to the gas phase. The combustion of aluminum produces aluminum oxide and releases heat and mass. The breakup of the particles affects the flowfield. It is known that a recirculation zone near the entry of the aft-dome cavity disturbs the flowfield and increases the complexity of interaction between the particle phase and the nozzle inlet section. This interaction will determine the slag agglomeration rate which affects the nozzle erosion and motor performance. All these impacts should be investigated so that a better performance of SRM can be achieved.

To provide design guides for maintaining high performance of the SRM, an accurate simulation of the gas-particle interaction is very important. Because of the complex flowfield inside the SRM, limited experimental data is available for design purposes. The internal flowfield analysis using CFD (Computational Fluid Dynamics) method can be utilized to obtain a better investigation for SRM due to the recent progress in computing power. There has been some research conducted in the past for the SRM internal flowfield analysis using the CFD method.

Madabhushi et al. (Ref. 1) calculated the two-phase aft-dome flowfield of the solid rocket motor. The 19-sec burnback configuration was used for the analysis and no particle trajectories in the aft-dome cavity was provided. This may not reveal the realistic particle effects for the first 19 seconds. Since the particles will accumulate on the wall and change the shape of the flow passage. Due to the large impact of turbulent particles, a full configuration

⁺ This research is sponsored by NASA Marshall Space Flight Center.

* Research Scientist, Engineering Sciences, Inc., Member AIAA.

** President, Engineering Sciences, Inc., Senior Member AIAA.

*** Project Monitor, NASA Marshall Space Flight Center

should be used to include the effect of upstream particles. Carrier et al (Ref. 2) investigated the aluminum-oxide-particle field within a long-bore SRM with a simple model. The Lagrangian particle tracking method was used in Ref. 2. Lupoglazoff and Vuillpt (Ref. 3) simulated the stability of a 2-D SRM numerically by means of finite volume explicit predictor-corrector McCormack scheme that solves the Euler equation. Sabnis et al (Ref. 4) used an Eulerian-Lagrangian two-phase approach to model the multi-phase reacting internal flow of a SRM with a metalized propellant. Other studies in solid propellant rocket motors have been conducted (Refs. 5-8). However, the realistic applications including the multi-phase flow with chemical reactions, evaporation, combustion, breakup, and agglomeration models were not simulated at the same time to investigate the influence of the particles on the SRM. No details about the effects of the recirculation zone on the motor performance have been revealed. Due to the complex flowfield at the entry of the cavity, more investigation for the aft-dome cavity should be conducted using the numerical approach, since it is very difficult to measure the data for the internal flow of the solid rocket motor. It is found that the slag behavior in the cavity causes the oscillated pressure and may affect the motor performance. Not many studies have been made to investigate the effects of the slag accumulation.

To explore the impacts due to the effects of chemical reaction, recirculation zone, slag behavior, and particle dynamics, a Navier-Stokes code, FDNS (Refs. 6-8), is used to analyze the complicated flowfield for the SRM with chemical reaction, and particle evaporation, combustion, breakup, and agglomeration models.

The objective of this study is to develop an advanced particulate multi-phase flow model which can simulate the effects of particle dynamics, slag accumulation, and gas flow turbulence for solid rocket motors. The inclusion of particle/gas reaction, mass transfer, and slag behavior in modeling the particle dynamics will allow the proposed models to realistically simulate the internal flowfield of a solid rocket motor.

NUMERICAL ANALYSIS

The FDNS flow solver is a finite difference method for solving non-linear governing equations using a non-staggered curvilinear grid system. This code provides multi-zone multi-block option for multiple species by solving the Navier-Stokes equations for the simulation of complex geometry flow problems. A Lagrangian-Eulerian particle tracking method is employed in the FDNS to provide effects of momentum and energy exchanges between the gas phase and the particle phase. The particle trajectories are calculated using a one-step implicit method for several groups of particle sizes by which the drag forces and heat fluxes are then coupled with the gas

phase equations. A second-order upwind scheme is employed to approximate the convection terms. Viscous fluxes and source terms are discretized using second-order central difference approximation. The time domain discretization of the present method allows the finite difference equations to be arranged into delta form for time accurate or steady-state computations respectively. A CFL number conditioned non-uniform time marching option can also be used for efficient steady-state solutions. The final linearized algebraic equations are solved by iterative point relaxation, ADI or L-U matrix solver.

The flowfield analysis using the FDNS code in the present research can provide a design guide for solid rocket motors. The obtained results can give the designer a basic guide line for the use of materials and the nozzle geometry. The investigation of the slag behavior in the aft-end cavity can assist the designer to improve the design of the RSRM geometry. The VOF (Volume of Fluid) method is employed to simulate the slag behavior in the aft-end cavity of the RSRM.

Governing Equations

The FDNS flow solver (Refs. 9-11) provides steady-state and unsteady flowfield solutions by solving the following transport equations. The general form of the mass conservation equation, Reynolds-averaged Navier-Stokes equations, energy equation and other scalar transport equations can be written as:

$$\frac{\partial \rho U}{\partial t} + \frac{\partial}{\partial x_i} \left(\rho u_i U + \mu_e \frac{\partial U}{\partial x_i} \right) = S_U \quad (1)$$

where ρ and $U = (1, u, v, w, h, k, \varepsilon \text{ and } \alpha_i)$ stand for the fluid density and the flow primitive variables for the continuity, momentum, energy, turbulence model and species mass-fraction equations respectively. This general form of the transport equation has one exception that fluid temperature instead of enthalpy is used for the diffusion (heat conduction) terms of the energy equation. The source terms S_U for the momentum, energy, turbulence model and species mass-fraction equations in 3-dimensional space x_i can be written for fully conservative form as:

$$S_U = \left\{ \begin{array}{l} M_p \\ -\frac{\partial P}{\partial x_j} + \frac{\partial}{\partial x_i} \left(\mu_e \frac{\partial u_i}{\partial x_j} \right) - \frac{2}{3} \frac{\partial}{\partial x_j} \left(\mu_e \frac{\partial u_i}{\partial x_i} \right) + D_i + M_p V_{p_i} \\ \frac{DP}{Dt} + \Phi + Q_t - V_{p_i} D_i + M_p (h\nu + U r^2 / 2) \\ \rho (P_r - \varepsilon) \\ \rho \frac{\varepsilon}{k} [(C_1 + C_3 P_r / \varepsilon) P_r - C_2 \varepsilon] \\ \omega_n, n = 1, \dots, N \end{array} \right\}$$

where $\mu_e = (\mu_l + \mu_t)/\sigma$ represents the effective viscosity which is a sum of the laminar viscosity and the turbulence eddy viscosity then divided by the Schmidt or Prandtl

number, σ . Φ , Q_t and ω_n are the energy dissipation function, heat source and the species source term respectively. D_i represent the drag forces. M_p denotes the rate of mass addition per unit volume due to inter-phase mass exchange. V_i are the particle velocity components. h_v stands for the particle vapor enthalpy. U_r is the gas velocity relative to the particle velocity. Pr stands for the turbulence kinetic energy production rate which is written as:

$$Pr = \frac{\mu_t}{\rho} \left\{ \frac{1}{2} \left(\frac{\partial u_j}{\partial x_i} + \frac{\partial u_i}{\partial x_j} \right)^2 - \frac{2}{3} \left(\frac{\partial u_k}{\partial x_k} \right)^2 \right\}$$

The turbulence modeling constants C_1 and C_2 are given as 1.43 and 1.92 respectively in the standard k- ϵ turbulence model. For the extended model, $C_2 = 1.90$ is a modeling constant and C_1 takes a functional form as:

$$C_1 = 1.15 + 0.25 \frac{Pr}{\epsilon}$$

Turbulence Schmidt numbers for the k- and ϵ -equation are 1.0 and 1.3 respectively for the standard model. For the extended model these two constants are modified to be 0.8927 and 1.15 respectively. Turbulence Schmidt number for the species mass fraction equation is assumed to be 0.9. The same value is assumed for the energy equation turbulence Prandtl number (0.7 is used for laminar flows). To account for compressibility effect on the turbulence models, two methods of model correction are available in the FDNS code. They are: (1) k-equation correction, in which the dissipation term in the k-equation is modified by a turbulence Mach number; and (2) ϵ -equation correction, in which the C_1 in the ϵ -equation is modified by the flow Mach number. An equation of state of the following form is used to calculate fluid density and provide closure to the above governing equations.

$$\rho = \frac{P}{RT / M_w}$$

where R , T and M_w stand for the universal gas constant, fluid temperature and the mixture molecular weight. The fluid temperature is calculated based on the solution of the fluid enthalpy and the JANNAF standard thermodynamics data using a Newton's iteration method for finding the roots of the polynomials.

Particulate-Phase Equations

The equations constitute the particle trajectory and temperature history can be written as:

$$\begin{aligned} DV_i / Dt &= (U_i - V_i) / t_d \\ Dh_p / Dt &= Cp_p (T_{aw} - T_p) / t_H - 6\sigma\epsilon f T_p^4 / (\rho d)_p \end{aligned}$$

where

- U_i = gas velocity
- V_i = particle velocity
- t_d = particle dynamic relaxation time
 $= 4\rho_p d_p / (3Cd\rho_c |U_i - V_i|)$
- h_p = particle enthalpy
- T_p = particle temperature
- T_{aw} = gas recovery temperature
- t_H = particle thermal-equilibrium time
 $= (\rho d)_p / [12 Nu \mu / (Pr d_p)]$
- σ = Stefan-Boltzmann constant
 $= 4.76E-13 \text{ BTU/FT}^2\text{-S-}^\circ\text{R}$
- ϵ = particle emissivity = 0.20 ~ 0.31
- f = radiation interchange factor

Cd and Nu stand for drag coefficient and Nusselt number for heat transfer which are functions of Reynolds number and relative Mach number. Typical correlation are described in references 12 and 13.

Numerical Algorithm

The FDNS flow solver is a finite difference method for solving non-linear governing equations using non-staggered curvilinear grid system. This code provides multi-zone multi-block option (Ref. 14) for multiple species and finite rate chemistry reacting flow by solving the Navier-Stokes equations for the simulation of complex geometry flow problems. A Lagrangian-Eulerian particle tracking method is employed in the FDNS to provide effects of momentum and energy exchanges between the gas phase and the particle phase. The particle trajectories are calculated using a one-step implicit method for several groups of particle sizes by which the drag forces and heat fluxes are then coupled with the gas phase equations. A second-order upwind scheme is employed to approximate the convection terms. Viscous fluxes and source terms are discretized using second-order central difference approximation. The time domain discretization of the present method allows the finite difference equations to be arranged into delta form for time-marching integration. Time-centered or Euler implicit time-marching schemes are employed for time accurate or steady-state computations respectively. A CFL number conditioned non-uniform time marching option can also be used for efficient steady-state solutions. The final linearized algebraic equations are solved by iterative point relaxation, ADI or L-U matrix solver. The time-marching scheme is described below. For convenience, transformed equation (from X_i to ξ_i system with J as the Jacobian of coordinate transformation) of Eq. 1 is written as:

$$\frac{1}{J} \frac{\partial \rho U}{\partial t} = - \frac{\partial F_i}{\partial \xi_i} + S_U = R_U \quad (2)$$

where F represents convection and diffusion fluxes. First, Eq. 2 is discretized in time with a second-order time-centered scheme. That is

$$\frac{1}{J\Delta t} \{ (\rho U)^{n+1} - (\rho U)^n \} = \frac{1}{2} (R_v^{n+1} + R_v^n)$$

where superscripts n and n+1 represent old and new time levels respectively. If a sub-iteration procedure within a time step is applied, the following linearization can be incorporated.

$$(\rho U)^{k+1} = (\rho U)^k + \rho^k \Delta U^k$$

$$R_v^{k+1} = \left(\frac{\partial R_v}{\partial U} \right)^k \Delta U^k + R_v^k$$

where the superscript k denotes the k-th sub-iteration. With the above approximations, the final form of the time-marching scheme can be written as:

$$\left\{ \frac{\rho^k}{J\Delta t} - \left(\frac{\partial R_v}{\partial U} \right)^k \right\} \Delta U^k = - \frac{(\rho U)^k - (\rho U)^n}{J\Delta t} + \frac{R_v^k + R_v^n}{2}$$

The solutions at time level n+1 is then updated by:

$$U^{n+1} = U^{k+1} = U^k + \Delta U^k$$

When k = 1 is selected, a non-iterative time-marching scheme with a multi-corrector solution method can provide time accurate solutions for unsteady flow problems. The pressure based multi-corrector solution method is formulated using simplified perturbed momentum and continuity equations. The simplified velocity correction equation can be written as:

$$\frac{\partial \rho u_i}{\partial t} \approx -\nabla P'$$

or, in discrete form,

$$u_i' \approx -\beta \frac{\Delta t}{\rho} \nabla P' \quad \text{and} \quad P^{n+1} = P^n + P' \quad (3)$$

where β represents a pressure relaxation parameter (typically 10). The velocity and density fields in the continuity equation are then perturbed to form a correction equation. Higher order terms are neglected. That is,

$$\frac{\partial \rho'}{\partial t} + \nabla(u_i \rho') + \nabla(\rho u_i') = - \left(\frac{\partial \rho}{\partial t} \right)^n - \nabla(\rho u_i)^n \quad (4)$$

Substituting Eq. 3 into 4 and letting $\rho' = P'/RT$, the following all speed pressure correction equation is obtained.

$$\frac{1}{RT} \frac{\partial P'}{\partial t} + \nabla \left(\frac{u_i}{RT} P' \right) - \nabla(\beta \Delta t \nabla P') = - \left(\frac{\partial \rho}{\partial t} \right)^n - \nabla(\rho u_i)^n \quad (5)$$

To provide smooth shock solutions the adaptive dissipation terms based on the pressure field is added to the right hand side of Eq. 5. Once solution of Eq. 5 is obtained, the velocity and pressure fields are updated using Eq. 3. The density field is then updated through the equation of state. The temperature field can also be modified by using a perturbed temperature correction equation. The entire corrector step is repeated 3 or 4 times such that the mass conservation condition is enforced before marching to the next time level.

VOF Model

The VOF (Volume Of Fluid, Refs. 21 and 22) method is used to account for the effect of slag accumulation in the aft end region. VOF method can be used to predict the sloshing dynamics, in response to the flight dynamics and local acceleration of the slag in the aft end region. Traditionally, VOF methods are mainly developed and used for low-speed flows such that incompressibility can be assumed. The incompressible flow assumption has limited their capability. To generalize, the present formulation is based on compressible flow governing equations. The forms of the equations are then continuously reduced to their incompressible forms according to the local flow conditions and the VOF solutions. To illustrate this, a general transport equation can be written as:

$$\frac{\partial \rho \phi}{\partial t} + \frac{\partial \rho (u - u_g)_i \phi}{\partial x_i} = S_\phi \quad (6)$$

And, the VOF transport equation is given below:

$$\frac{\partial \alpha}{\partial t} + (u - u_g)_i \frac{\partial \alpha}{\partial x_i} = S_\alpha$$

where $\alpha = 1$ stands for liquid and $\alpha = 0$ is for gas. The interface is located at $1 > \alpha > 0$. For a given solution of α field, equation (6) can be recast as:

$$\frac{\partial \rho_m \phi}{\partial t} + \frac{\partial \rho_m (u - u_g)_i \phi}{\partial x_i} = S_\phi, \alpha < 0.01, \text{ for compressible gas}$$

$$\rho_m \frac{\partial \phi}{\partial t} + \rho_m (u - u_g)_i \frac{\partial \phi}{\partial x_i} = S_\phi, \alpha \leq 0.01, \text{ for compressible gas}$$

and

$$\rho_m = \text{Max} \{ \rho_g, \alpha \rho_l \}$$

where ρ_g and ρ_l denote gas and liquid density respectively. u_g represents the grid speed components used to simulate moving domain effects. The numerical accuracy of the VOF method depends highly on the interface resolution. To prevent the solution from becoming too smearing due to numerical diffusion, a compression procedure is developed to perform VOF interface rescaling such that the total volume within the interface ($0.1 < \alpha < 0.9$) is kept constant through out the computation. The interface α solution compression procedure is expressed as:

$$\alpha_{new} = \text{Max} \left\{ 0, \text{Min} \left[1, 0.5 + f(\alpha_{old} - 0.5) \right] \right\}$$

and

$$f = \frac{(\text{Interface volume})_{new}}{(\text{Interface volume})_{initial}}$$

The surface tension forces in the continuum surface force model is formulated as continuous body forces across the interface. These forces can be written as:

$$\begin{aligned} F_x &= -\sigma \left(\nabla \hat{n} \right) \alpha_x \\ F_y &= -\sigma \left(\nabla \hat{n} \right) \alpha_y + \left(\frac{|\alpha_y|}{y} \right), \text{ for 2D, axisymmetric case only} \\ F_z &= -\sigma \left(\nabla \hat{n} \right) \alpha_z, \text{ for 3D case only} \end{aligned}$$

where

σ = surface tension constant

$$\nabla \hat{n} = \hat{\alpha}_{xx} + \hat{\alpha}_{yy} + \hat{\alpha}_{zz}$$

α is 0.5 for the free surface. The VOF method is used to represent the tracking of the free surface between the liquid and gas phase.

NUMERICAL RESULTS

A 2-D grid system of 5,735 grids (Fig. 1) simulating the axisymmetric RSRM configuration was tested to investigate the slag behavior in the aft-end cavity. To simulate a more realistic flight condition, an initial volume of accumulated slag is assumed in the cavity at 67 seconds. The assumed volume of the slag occupies half of the space of the aft-end cavity. A group of particles with diameter of 100 μm is used to simulate the particular phase. It is noted that only the configuration near the aft-end cavity is simulated to investigate the slag behavior. No chemical reaction and turbulent particle dispersion analysis are included for this study. No evaporation, combustion, breakup, and agglomeration models are applied. Only the qualitative analysis is

attempted. In order to make comparisons, the RSRM configuration is tested first without particles to simulate the gas phase. The effects of the particles are then simulated to investigate the slag behavior.

Without particles

Figures 2, 3, and 4 show the contours of Mach number, pressure, and temperature, respectively. Smooth distributions are obtained without the effects of particles. Maximum pressure is 619psi. Maximum temperature is 6,137°R. Figure 5 illustrates the velocity vectors in the aft-end cavity without particles. The vortex and an impinging stagnation point on the wall are predicted. This is due to the large flow velocity difference between the chamber and the cavity. The predictions of the flowfield near the cavity are reasonable based on the physical point of view.

With particles

Figure 6 shows that the molten particles may enter the cavity and accumulate on the wall. The particle impingement could cause the erosion and damage the nozzle wall. The particles may accumulate in the impingement area and change the wall shape and then affect the performance of the motor. The accumulation of the slag in the aft-end cavity may affect the performance of the solid rocket motor. The flowfields are disturbed by the particles and the slag. The phenomenon is reasonable based on the physical point of view and available experimental data.

The accumulation of slag may occur depending on the temperature, the vortex strength, and the flight angle. The shape of the aft-end cavity dominates the shape and strength of the vortex. Apparently, the slag accumulation exist in the aft-end cavity as soon as the propellant burns in the aft-end cavity. In order to investigate the effects of the particle size on the slag accumulation, different particle diameters are used for this purpose. Figure 7 demonstrates that the slag flow rate entering the cavity depends on the particle size. It shows that an efficient particle combustion results in a less slag accumulation in the aft-end cavity. The effects of the particles on the Mach number and temperature contours are shown in figures 8 and 9, respectively. The contours are affected strongly by the particle concentration.

The slag accumulation in the aft-end cavity will change the particle concentration and affects the flowfield. Figure 10 illustrates this phenomenon. The slag accumulation in the aft-end cavity at different time is shown in Fig. 10. It clearly demonstrates the effects of the slag on the flowfields. Figure 10(1) shows the initial conditions of the assumed slag accumulation and the particle trajectories near the cavity at $t = 0$ second. It shows that the particles impinge on the wall near the entry of the lower surface of the cavity. The slag should

accumulate in this area. Figure 10(2) (at $t = 0.000444$ sec) demonstrates this predicted phenomenon. It is seen that particles accumulate on the wall and form the slag layer. The flowfield will then be disturbed due to this slag accumulation. Figure 10(3) illustrates that more slag accumulated in the cavity at $t = 0.0598$ sec. The slag accumulated on the upper surface of the cavity. It also shows that the slag accumulation in the cavity apparently changes the flowfield of the aft-end cavity. Figure 10(4) shows that the slag starts to flow out of the cavity along the wall at $t = 0.3482$ sec. The particle concentration near the entry of the nozzle is changed by the slag. The slag in the cavity moves due to the oscillated acceleration. More slag comes out of the cavity as shown in figures 10(5)-(8). The slag grows by the merge of the particles coming from the chamber. It is shown that the particle trajectories change due to the effects of the slag accumulation. The slag on the upper surface of the cavity moves due to the effects of the flowfield and the acceleration of the flight (also see figures 10(5)-(8)). The slag will finally enter the nozzle and affect the performance of the solid rocket motor.

CONCLUSIONS AND DISCUSSION

The obtained computational results using FDNS with the proposed models demonstrate the complex internal flowfields of solid rocket motors. The prediction of the recirculation zone in the aft-dome cavity, the particle impingement on the wall, the effects of the particles on the flowfield, and the slag behavior in the aft-end cavity are very crucial for the improvement of the solid rocket motor performance. The predicted results are comparable to the known design values and the flowfield is reasonable based on the physical point of view.

The flowfield analysis using the FDNS code in the present study can provide a design guidance for the solid rocket motors. Especially, the obtained results can provide the designers a basic guide line for the use of materials and the design of the geometry. The analysis of the slag behavior plays an important role for the SRM design, since the distribution of the slag changes the flowfield at the entry of the nozzle and affects performance of the motor. A better performance of the solid rocket motor can be achieved by modifying the geometry of the aft-end cavity using the CFD method to prevent the formation of vortex and slag accumulation in the aft-end cavity. The geometry of the propellant grain can also be modified using the CFD method to increase the combustion efficiency.

REFERENCES

1. Madabhushi, R., Sabnis, J., Jong, F., and Gibeling, H., "Calculation of the Two-Phase Aft-Dome Flowfield in Solid Rocket Motors," *Journal of Propulsion*, Vol. 7, NO. 2, March-April 1991, pp. 178-184.
2. Carrier, G., Fendell, F., Brent, D., Kimbrough, C., Loucks, S., Hess, E., and Acotsa, P., "Simple Modeling of Particle Trajectories in Solid Rocket Motors," *J. of Propulsion*, Vol. 7, NO. 2, March-April, 1991, pp. 185-195.
3. Lupoglazoff, N., and Vuillot, F., "Two-Dimensional Numerical Simulation of the Stability of A Solid Propellant Rocket Motor," AIAA-91-0205, AIAA 29th Aerospace Science Meeting, Reno, Nevada, Jan. 1991.
4. Sabnis, J., Jong, F. de, and Gibeling, H., "A Two-Phase Restricted Equilibrium Model for Combustion of Metalized solid Propellants," AIAA-92-3509, AIAA/SAE/ASME/ASEE 28th Joint Propulsion Conference and Exhibit, Nashville, TN, July 6-8, 1992.
5. Hsieh K., Yang, V., and Tseng, I., "Navier-Stokes Calculation of Solid Propellant Rocket Motor Internal Flow Fields," AIAA-88-3182, AIAA 24th Joint Propulsion Conference, Boston, July 1988.
6. Culick, F. E. C., "Rotational Axisymmetric Mean Flow and Damping of Acoustic Waves in a Solid Propellant Rocket," *AIAA Journal*, Vol. 4, No. 8, 1966, pp. 1462-1469.
7. Chang, I., "An efficient Solution for Viscous Flow Inside SRM," AIAA Paper 91-2429, June 1991.
8. Golafshani, M. and Loh, H. T., "Computation of Two-Phase Viscous Flow in Solid Rocket Motors Using a Flux-Split Eulerian-Lagrangian Technique," AIAA Paper 89-2785, July 1989.
9. Chen Y.-S., "Compressible and Incompressible Flow Computations with a Pressure Based Method," AIAA Paper 89-0286, AIAA 27th Aerospace Sciences Meeting, Reno, Nevada, Jan. 1989.
10. Chen Y.-S., "Viscous Flow Computations Using A Second-Order Upwind Differencing Scheme," AIAA Paper 88-0417, AIAA 26th Aerospace Sciences Meeting, Reno, Nevada, Jan. 11-14, 1988.
11. Wang T.-S. and Chen, Y.-S., "A Unified Navier-Stokes Flowfield and Performance Analysis of Liquid Rocket Engines," AIAA Paper 90-2494, AIAA/SAE/ASME/ASEE 26th Joint Propulsion Conference, Orlando, FL, July 16-18, 1990.
12. Carlson, D., and Hoglund, R., *AIAA Journal*, Vol. 2, NO. 11, Nov. 1964.
13. Henderson, C., *AIAA Journal*, Vol. 14, NO. 6, June 1976, p. 707.
14. Rhie, C. M., "A Pressure Based Navier-Stokes Solvers Using the Multigrid Method," AIAA Paper 86-0207, AIAA 24th Aerospace Sciences Meeting, Jan. 1986.

15. Hermesen, R. W., "Aluminum Combustion Efficiency in Solid Rocket Motors," AIAA paper 81-0038, January 1981.
16. Spalding, D. B., Proc. 4th Symposium (International) on Combustion, William and Wilkins, Baltimore, MD (1953) 847-864.
17. Caveny, L. H. and Gany, A., "Breakup of Al/Al₂O₃ Agglomerates in Accelerating Flowfields," AIAA Journal, Vol. 17, No. 12, Dec. 1979.
18. Smithells, C. J., "Metal Reference Book," Vol. II, 3rd ed., Butterworth & Co., Ltd., London, 1962, p. 685.
19. Brandt, J. L., "Properties of Pure Aluminum," *Aluminum, Vol. 1 Properties, Physical Metallurgy and Phase Diagrams*, edited by K. R. Van Horn, American Society for Metals, Metals Park, Ohio, 1967, pp. 18-19.
20. Harje, D. T. and Reardon, F. H., Eds., "Liquid Propellant Rocket Combustion Instability," NASA SP-194, 1972.
21. Hirt, C. W., and Nichols, B. D., "Volume of Fluid (VOF) Method for the Dynamics of Free Boundaries," Journal of Computational Physics, Vol. 100, pp. 335 - 354, 1992.
22. Nichols, B. D., Hirt, C. W., and Hotchkiss, R. S., "SOLA-VOF: A Solution Algorithm for transient Fluid Flow with Incompressible Flows with Free Surfaces," Los Alamos Lab., LA-8355, Aug., 1980.
23. Price, E. W., "Combustion of Metallized Propellants," Progress in Astronautics and Aeronautics; Fundamentals of Solid Propellant Combustion, Vol. 90, AIAA, New York 1984, PP. 479-513

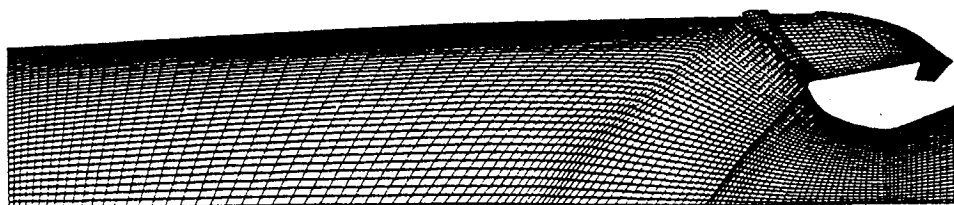


Figure -1 2D Grid system of RSRM configuration.

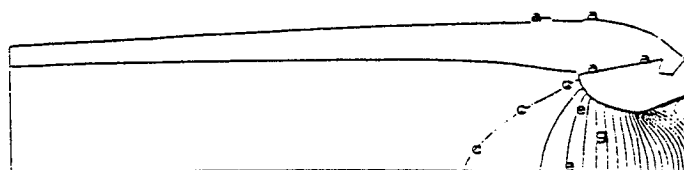


Figure -2 Mach number contours of RSRM, no particles.

Color-Map
0 0000E+00
1 3244E-02
2 6348E-01
3 4973E-01
4 3297E-01
5 1522E-01
6 8846E-01
7 8370E-01
8 8359E-01
9 4919E-01
10 3244E-01
11 1588E-01
12 8888E-01
13 8821E+00
14 1E34E+00
15 2488E+00
16 3319E+00
17 4151E+00
18 4988E+00
19 5816E+00
20 6648E+00
21 7481E+00
22 8313E+00
23 9146E+00
24 9978E+00
25 1081E+00

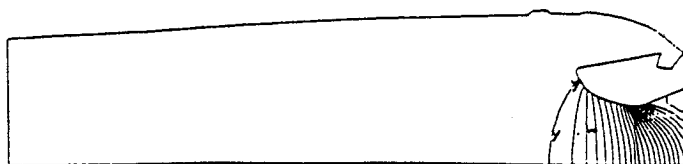


Figure -3 Pressure contours of RSRM, no particles.

Color-Map
4 9612E+00
5 4488E+00
6 9364E+00
7 4241E+00
8 8811E+01
9 2398E+01
10 3888E+01
11 5374E+01
12 6862E+01
13 8348E+01
14 9837E+01
15 1325E+01
16 2812E+01
17 4300E+01
18 5787E+01
19 7275E+01
20 8763E+01
21 10250E+01
22 11738E+01
23 13226E+01
24 14713E+01
25 16201E+01
26 17688E+01
27 19176E+01
28 20664E+01
29 22151E+01

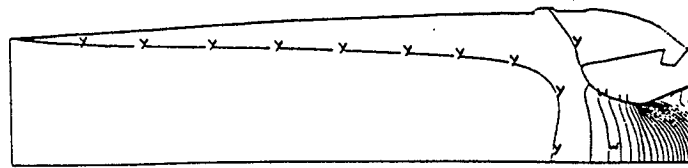


Figure 4 Temperature contours of RSRM, no particles.

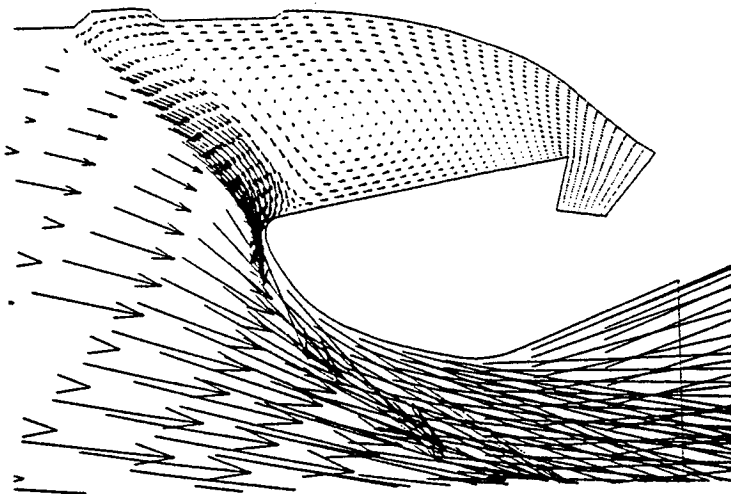


Figure 5 Velocity vectors near the aft-end cavity, no particles.

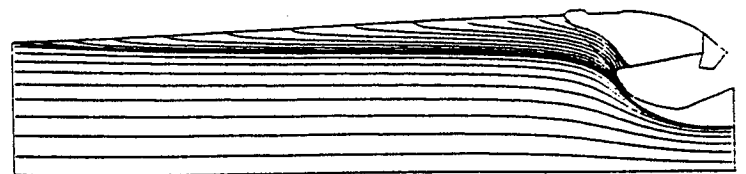


Figure 6 Particle trajectories.

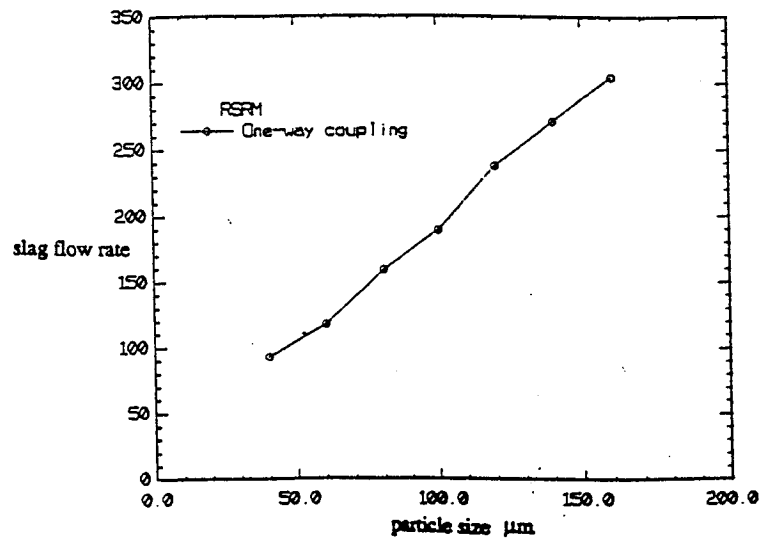


Figure 7 Slag flow rate entering the aft-end cavity v.s. particle sizes.

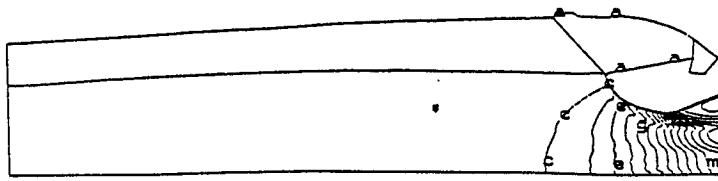


Figure 8 Mach number contours of RSRM, with particles.

0.0000E+00
9.4611E-02
1.6922E-01
2.8383E-01
3.7844E-01
4.7305E-01
5.6766E-01
6.6227E-01
7.5688E-01
8.5150E-01
9.4611E-01
1.0407E+00
1.1353E+00
1.2299E+00
1.3245E+00
1.4191E+00
1.5137E+00
1.6083E+00
1.7030E+00
1.7976E+00
1.8922E+00

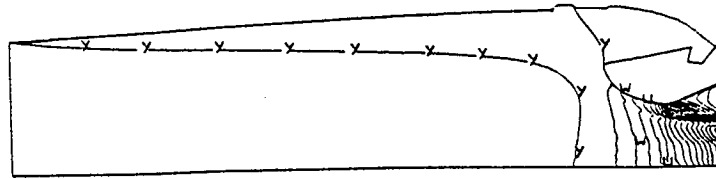
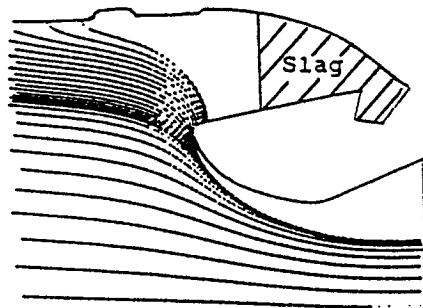
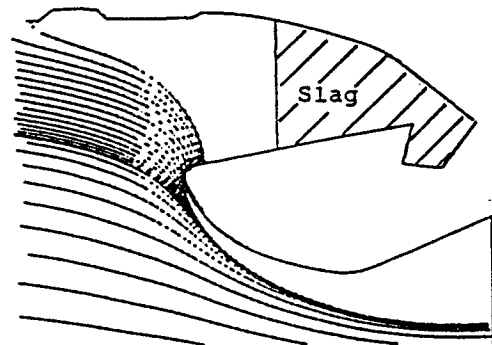


Figure 9 Temperature contours of RSRM, with particles.

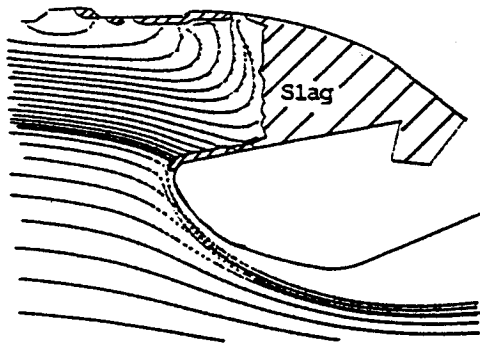
4.1296E+03
4.2055E+03
4.2902E+03
4.3705E+03
4.4508E+03
4.5310E+03
4.6113E+03
4.6916E+03
4.7719E+03
4.8522E+03
4.9325E+03
5.0128E+03
5.0930E+03
5.1733E+03
5.2536E+03
5.3339E+03
5.4142E+03
5.4945E+03
5.5747E+03
5.6550E+03
5.7353E+03
5.8156E+03
5.8959E+03
5.9762E+03
6.0565E+03
6.1367E+03



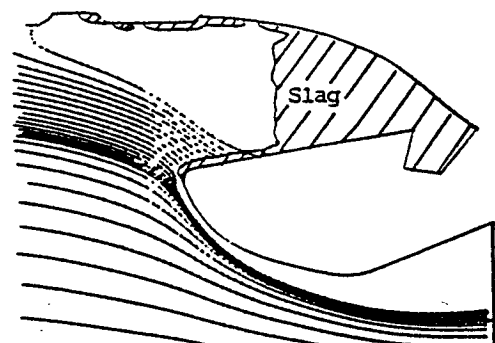
(1) $t=0.0$ sec.



(2) $t=0.000444$ sec.

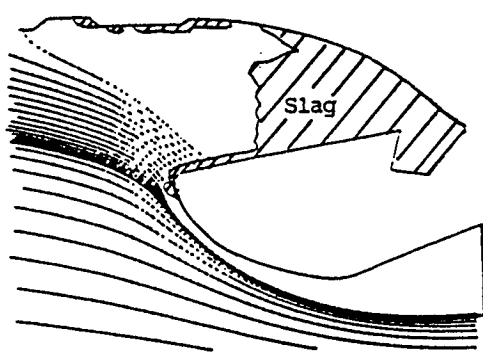


(3) $t=0.0598$ sec.

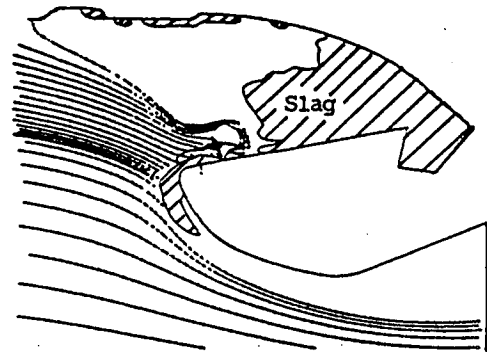


(4) $t=0.3482$ sec.

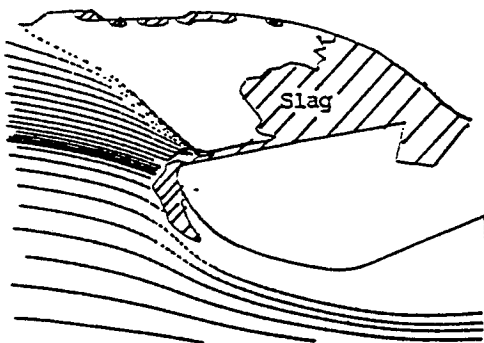
Figure 10 Slag buildup history in the aft-end cavity.



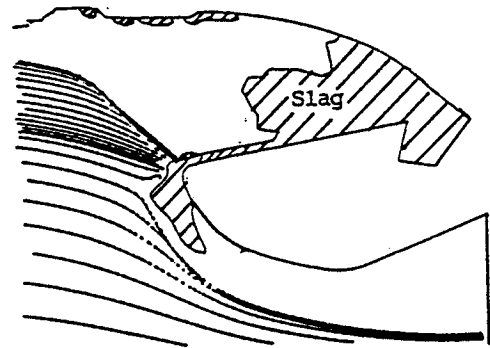
(5) $t=1.9585$ sec.



(6) $t=4.7209$ sec.



(7) $t=5.3609$ sec.



(8) $t=6.2115$ sec.

Figure 10 (continued) Slag buildup history in the aft-end cavity.